Article

Improving Deforestation Detection on Tropical Rainforests Using Sentinel-1 Data and Convolutional Neural Networks

Mabel Ortega Adarme [1,*] **, Juan Doblas Prieto** [2] **, Raul Queiroz Feitosa** [1]
and Cláudio Aparecido De Almeida [2]

1   Department of Electrical Engineering, Pontifical Catholic University of Rio de Janeiro,
    Rio de Janeiro 22451-900, Brazil; raul@ele.puc-rio.br
2   National Institute for Space Research (INPE), São Jose dos Campos, São Paulo 12227-010, Brazil;
    juan.doblas@inpe.br (J.D.P.); claudio.almeida@inpe.br (C.A.D.A.)
*   Correspondence: mortega@aluno.puc-rio.br

Abstract: Detecting early deforestation is a fundamental process in reducing forest degradation and carbon emissions. With this procedure, it is possible to monitor and control illegal activities associated with deforestation. Most regular monitoring projects have been recently proposed, but most of them rely on optical imagery. In addition, these data are seriously restricted by cloud coverage, especially in tropical environments. In this regard, Synthetic Aperture Radar (SAR) is an attractive alternative that can fill this observational gap. This work evaluated and compared a conventional method based on time series and a Fully Convolutional Network (FCN) with bi-temporal SAR images. These approaches were assessed in two regions of the Brazilian Amazon to detect deforestation between 2019 and 2020. Different pre-processing techniques, including filtering and stabilization stages, were applied to the C-band Sentinel-1 images. Furthermore, this study proposes to provide the network with the distance map to past-deforestation as additional information to the pair of images being compared. In our experiments, this proposal brought up to 4% improvement in average precision. The experimental results further indicated a clear superiority of the DL approach over a time series-based deforestation detection method used as a baseline in all experiments. Finally, the study proved the benefits of pre-processing techniques when using detection methods based on time series. On the contrary, the analysis revealed that the neural network could eliminate noise from the input images, making filtering innocuous and, therefore, unnecessary. On the other hand, the stabilization of the input images brought non-negligible accuracy gains to the DL approach.

Keywords: deep learning; deforestation detection; stabilization; synthetic aperture radar; time series; tropical rainforest

1. Introduction

Tropical forests are one of the most biodiverse ecosystems on Earth, comprising the most significant portion of terrestrial species in the world. Unfortunately, in the last decades, with the growth of industrial development, renewable and nonrenewable natural resources have accelerated alarmingly, which has been reflected in severe environmental changes, including forest loss and degradation [1,2]. A particularly critical situation is the constant deforestation process in the Brazilian Legal Amazon (BLA). This region covers an area of approximately 5,200,000 km^2 and represents over 59% of Brazil's land mass [3]. Therefore, the increase in the deforestation rates could lead to irreversible alterations in this tropical region, such as the greenhouse effect, soil erosion, and climate change [1,4–7].

Remote sensing (RS) has been crucial in environmental research [8], especially in monitoring forest ecosystems. With the extensive advance of these technologies and the increase in the availability of satellite images in short revisit times, it is possible to monitor forest loss processes efficiently and timely [6]. Several global and national deforestation

monitoring systems based on optical satellite data are currently operational [9]. For instance, Forest Alerts dataset of Global Land Analysis & Discovery (GLAD [10]) employs Landsat data and monitors areas of Peru, Brazil, Central Africa, and a portion of South Asia. In Brazil, the DETER-B system [11], developed and executed by the Brazilian National Institute for Space Research (INPE), monitors deforestation continuously using WFS images of the CBERS-4 satellite. Nevertheless, due to the cloud cover, the monitoring of a larger portion of the biome is severely hampered, notably during the rainy season.

In this context, Synthetic Aperture Radar (SAR) sensors are an attractive alternative data source alternative to optical images. Active sensors can provide cloud-free observations and the capacity to operate almost regardless of weather and atmospheric conditions state [12]. Moreover, most SAR satellites currently operate with short revisit times, which would allow an effective Early Warning System (EWS) for deforestation processes [9]. In fact, EWS has played a fundamental role in reinforcing governmental policies that have led to a significant decrease in deforestation rates in Brazil [13–15].

Numerous research projects have been proposed to explore the potential of Sentinel-1 data for deforestation mapping and land cover monitoring in tropical regions [16–18]. Some of them based on Bayesian classification [19–21] or multiple thresholding [22] of time series. Others rely on conventional machine learning approaches such as Random Forest, Support Vector Machine, k-Nearest-Neighbors, and Quadratic Discriminant Analysis [23–26]. However, manual feature extraction and pre-processing stages are required for these methods. Furthermore, time series methods produce classification results using a large quantity and quality of classified images [27], which generally implies computationally complex processes. In addition, they have a variety of calibration criteria that make it difficult to monitor deforestation events effectively and quickly, and they rely largely on seasonality in the time series [8].

However, the use of SAR data for deforestation detection is hampered by two main factors: speckle noise and the susceptibility of the backscatter signal to variations in canopy and soil moisture. The speckle noise reduces radiometric resolution and negatively impacts interpretation and classification [8]. While the research on methods for attenuating speckle noise is already well established (e.g., [28–31]), solutions for SAR signal instability due to vegetation/soil moisture are still subject of research.

A recent publication [20] evaluated different SAR data stabilization and filtering algorithms for detecting deforestation in the Amazon rainforest. The article reports significant accuracy gains when the SAR data are first applied to such pre-processing operations before being applied to a classification method based on multiple time series thresholds. Furthermore, in [19], time-series data from different radar sensors, including Sentinel-1, RADARSAT-2, and Advanced Land Observing Satellite-2 Phased Arrayed L-band Synthetic Aperture Radar-2 (ALOS-2 PALSAR-2) were evaluated for monitoring tropical selective logging. Nevertheless, the SAR data requires a prior pre-processing stage before being classified by traditional methods such as maximum likelihood and random forest models.

Deep Learning (DL) has become prevalent in the last few years, including RS [32–34], due to its unprecedented success in many application fields. This success stems from DL's ability to learn discriminative representations directly from raw data [35], often giving up the pre-processing steps and handcrafted representations typically required in traditional Machine Learning methods. Regarding deforestation detection, novel DL-based approaches have been recently proposed for deforestation detection, most of them relying on optical imagery [36–38]. In addition, some works using SAR and DL architectures have also been proposed. For instance, Silva et al. [39] employed SAR data with a Multi-Layer Perceptron (MLP) to detect forest disturbances in near-real-time. In this methodology, a set of statistical parameters of backscatter coefficients are computed and used as input to the network. Similarly, Neitzel et al. [40] evaluate several pretrained DL architectures to detect selective logging using different scores of contextual and textural information from X-Band SAR data and compose an RGB composition. Wahab et al. [41] also used a Convolutional Neural Network (CNN) to map deforestation using Sentinel-1 data. In this study, the Principal

Component Analysis (PCA) is applied to the Gray-Level Co-occurrence Matrix (GLCM) features of VH and VV polarizations, and the result is used as the input for the CNN.

In this scenario, one can question whether the pre-processing usually adopted in Machine Learning-based deforestation detection methods would also improve a solution based on fully convolutional networks and, if so, how much. The present study addresses this issue and aims to assess the potential accuracy gains brought about by stabilization and filtering techniques, such as those proposed in [20], for detecting deforestation in an FCN-based scheme.

A further aspect addressed by this study was motivated by the empirical observation that deforestation is more frequent in sites close to previously deforested areas. Thus, this study's second objective is to test whether the proximity of deforested spots increases the deforestation probability in the forested regions. Specifically, we propose to provide the network, in addition to the pair of images being compared, with a matrix containing the distance from each pixel to the nearest deforested point. Finally, this paper reports the results of our experiments to test this hypothesis.

The main contributions of this work are:

- An analysis of the effect caused by applying pre-processing techniques such as stabilization and filtering to the original Sentinel-1 data.
- A proposal of providing the convolutional network with the distance map to the nearest past-deforestation spot.
- An evaluation and comparison of two automatic methods applied to deforestation detection in two sites of the Brazilian Legal Amazon. The first one is a traditional method based on time series; the second one is based on Deep Learning techniques.

The remainder of this paper is structured as follows: Section 2 briefly introduces the pre-processing strategies applied to the input SAR data, the study areas, the deforestation detection methods, and the experimental protocol. Next, the experimental results are explained and analyzed in Section 3. Finally, the conclusions and final remarks are presented in Section 4.

2. Materials and Methods

This section presents the sites represented in the datasets, the evaluated methods, the pre-processing and the experimental setup employed in this study. We used a conventional method based on time series and a DL method with an FCN architecture for comparison purposes.

2.1. Datasets

This study relied on SAR data from two sites within the Brazilian Legal Amazon (see Figure 1), with geographical coordinates presented in Table 1. The first one is located in the Pará state and extends over 115×186 Km^2. The second one is located in Mato Grosso state and has an area of 104×138 Km^2. Both sites have a mixed land cover, mainly composed of dense evergreen forest and pastures in Pará, and dense forest, soy fields and pastures in Mato Grosso.

Table 1. Geographical coordinates of the Para and the Mato Grosso sites.

Point	Para	Mato Grosso
1	Lat: 3°14′25″S, Lon: 52°27′09″W	Lat: 11°49′21″S, Lon: 57°47′34″W
2	Lat: 3°14′29″S, Lon: 50°46′24″W	Lat: 11°49′23″S, Lon: 56°31′17″W
3	Lat: 4°17′06″S, Lon: 50°46′24″W	Lat: 12°46′03″ S, Lon: 56°31′11″W
4	Lat: 4°17′00″S, Lon: 52°27′15″W	Lat: 12°46′01″S, Lon: 57°47′44″W

According to statistics from PRODES project [42], Pará recorded the highest deforestation rate in 2020, followed by Mato Grosso, representing nearly 45% and 16% of the total forest loss over BLA. Table 2 presents the number of pixels and its percentage corresponding to the classes: deforestation, no deforestation, and past-deforestation for both

sites. It is worth noticing that both datasets are highly unbalanced, containing fewer pixels of the class deforestation, especially in Mato Grosso, where only 0.6% of the total area was deforested.

Table 2. Class distribution of deforestation, no deforestation, and past-deforestation in terms of number of pixels and percentage for Pará and Mato Grosso sites.

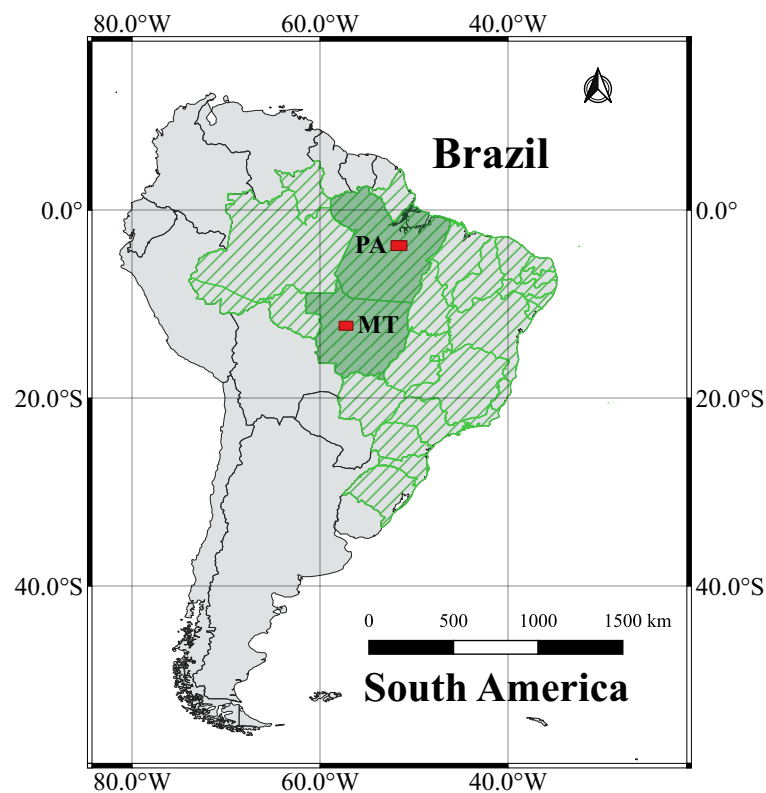| Class	Para		Mato Grosso	
	# of Pixels	Percentage (%)	# of Pixels	Percentage (%)
Deforestation	572,765	1.06	222,799	0.62
No deforestation	34,903,847	64.89	23,115,578	63.82
Past-deforestation	18,312,197	34.04	12,881,067	35.56

Figure 1. Geographical location of the study areas within the Pará (PA) and Mato Grosso (MT) Brazilian states.

The input datasets consist of Sentinel-1 GRD C-Band SAR images obtained and pre-processed using the Google Earth Engine (GEE) platform [43]. The standard initial preprocessing consisted of five steps, namely: (1) Apply orbit file, (2) GRD border noise removal, (3) Thermal noise removal, (4) Radiometric calibration, and (5) Terrain correction using SRTM terrain data. The Pará and Mato Grosso images comprised 5766×9320 pixels and 5230×6924 pixels, respectively.

Table 3 informs the relative orbit, slice number, and the image acquisition dates of Para and Mato Grosso sites, which correspond to the deforestation that occurred between the end of July 2019 ($Ref.T_0$) and the end of July 2020 ($Ref.T_1$), according to the 2020 PRODES report. The reference of the deforestation map is available on the INPE website, at the PRODES database [44].

Table 3. Relative orbit, slice number, and acquisition dates of the Sentinel-1 images.

Site	Relative Orbit	Slice Number	Adquisition Date	
			2019	**2020**
Pará	68	5	9 August 2019	3 August 2020
Mato Grosso	39	10	26 July 2019	13 August 2020

2.2. Distance Map to the Closest Deforestation

The present study proposes the distance to the nearest past-deforestation as an additional feature to the bi-temporal image pair. Consider a binary past-deforestation mask, indicating at each pixel position whether or not deforestation had already occurred up to the acquisition date of earliest between the pair of images being analyzed. This feature map is computed by the Euclidean distance transform given in (Equation (1)) below:

$$y_i = |\mathbf{x}_i - \mathbf{p}_i| \tag{1}$$

where y_i is the feature value assigned to the pixel i, $\mathbf{x}_i$ denotes its spatial coordinate vector, and $\mathbf{p}_i$ of its nearest pixel within the past-deforestation mask. The distance matrix is normalized using the min-max procedure and concatenated to the image pair along the polarization dimension. Figures 2 and 3 illustrate the past-deforestation map obtained from the PRODES database and the distance map generated for Pará and Mato Grosso sites, respectively. Points 1–4 correspond to the geographical location points defined in Table 1. Blue and red colors represent the nearest and more distant pixels from the forest to the nearest past-deforestation based on the PRODES datasets.
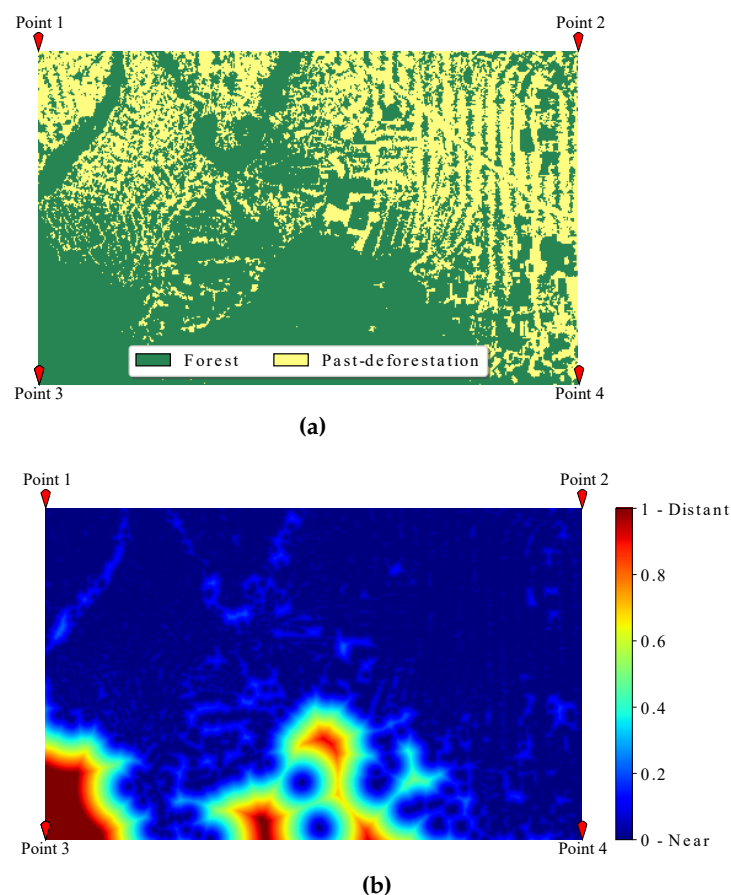

(a)

(b)

Figure 2. Past-deforestation and distance maps for the Pará site. Blue and red represent the nearest and more distant pixels from the forest to the nearest past deforestation. (**a**) Past-deforestation in the Pará site. (**b**) Distance map to the nearest past-deforestation for the Pará site.
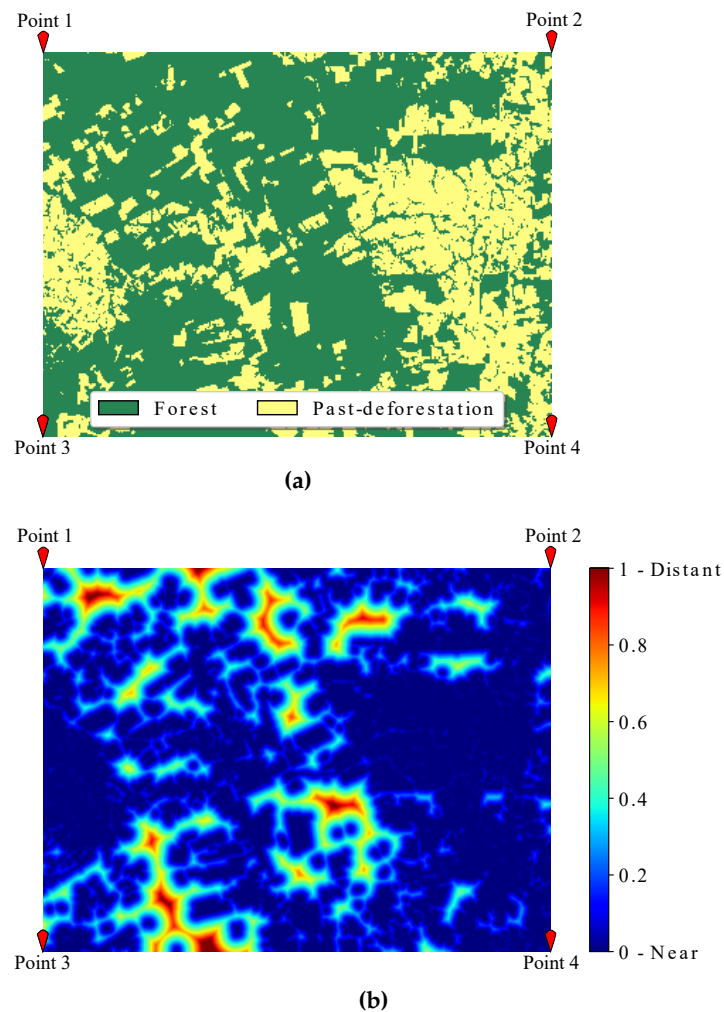
(a)

(b)

Figure 3. Past-deforestation and distance maps for the Mato Grosso site. Blue and red represent the nearest and more distant pixels from the forest to the nearest past-deforestation. (**a**) Past-deforestation of the Mato Grosso site. (**b**) Distance map to the nearest past-deforestation for the Mato Grosso site.

2.3. Preprocessing

The radar images can be pre-processed using speckle filters and different stabilization techniques to avoid false positives due to the speckle phenomena and the seasonal variability of the radar time series, as detailed in the following.

2.3.1. Stabilization

We adopted in this study the methodology originally proposed in [45] and also applied in [20]. The original images are pre-processed to remove the harmonic seasonality component. This treatment can help reduce variations in radar signals related to variations in the canopy moisture throughout the year. This study considered three years VH and VV time series for every pixel and fitted a time-dependent harmonic function to the backscattering values. In our case, the time series was composed of 88 images. For every pixel of every image, the corresponding value of the sinusoidal function is subtracted from the original pixel value to compute the stabilized pixel value. According to [20], although computationally challenging, harmonic stabilization can be rewarding if used in areas influenced by heavy precipitations.

2.3.2. SAR Image Despeckling

Speckle reduction is a standard procedure for SAR data processing. It aims to raise the signal-to-noise ratio and ease the interpretation of radar images. In this work, we employed

a traditional standard despeckling system, which uses two filters, applied sequentially: a temporal filter (Quegan and Yu) and a spatial filter (Refined Lee 7 × 7 filter).

We first apply the temporal filter [46] to a given SAR image based on a sequence of past coregistered images. To obtain the filtered outcome, we compute next the following expression:

$$J_k = \frac{\hat{\sigma}_k}{M} \sum_{i=1}^{M} \frac{I_i}{\hat{\sigma}_i} \tag{2}$$

where J_k is the filtered image, M the total number of collected images, I_i is the i-th image and $\hat{\sigma}_k = (1/N) \sum_{i=1}^{N} I_i^{(k)}$ is the spatial average over a NxN window centered around the current (x, y) position in the image k. $I_i^{(k)}$ refers to the pixels in this window.

After applying the temporal filter and following [46], we used a refined version [47] of Lee filter [48] due to its ability to preserve and enhance the edgy features of the input images. The original Lee filter is based on the statistical modeling of speckle and uses local statistics to reduce noise by applying the following expressions:

$$J = \langle I \rangle + k(I - \langle I \rangle) \tag{3}$$

where

$$k = \frac{Var(I)}{\langle I \rangle^2 \sigma_v^2 + Var(I)} \tag{4}$$

$$\sigma_v = \sqrt{Var(I)/\langle I \rangle} \tag{5}$$

J and I are the filtered and the original images, respectively, $\langle I \rangle$, and $Var(I)$ are the mean and variance of the original image over a 7 × 7 window, and σ_v is the standard deviation of the speckle, which can be approximated to $\sqrt{Var(I)/\langle I \rangle}$.

The refined version of the Lee filter looks for edges on the 7 × 7 filtering window. It then reshapes it depending on the edge orientation, thus reducing the number of pixels involved in the filtering process and reducing the noise variance.

The combination of the described temporal and spatial filters can effectively reduce noise and increase detection accuracy, but this comes at the expense of a heavy computational burden, mainly due to the high number of images taken into account during the temporal filter step.

Thus, to evaluate the performance and need for the temporal filtering, two different filtering treatments were defined and assessed: F_1, which only applies the spatial filter and F_2, which uses the complete filtering chain (temporal + spatial despeckling).

Figure 4 shows how SAR preprocessing affects both the input images and the results of the deforestation detection.

2.4. Pixel Labeling

This section describes the two automatic methods evaluated in this work for deforestation detection. The first is a conventional method based on time series, while the second relies on a deep learning approach.
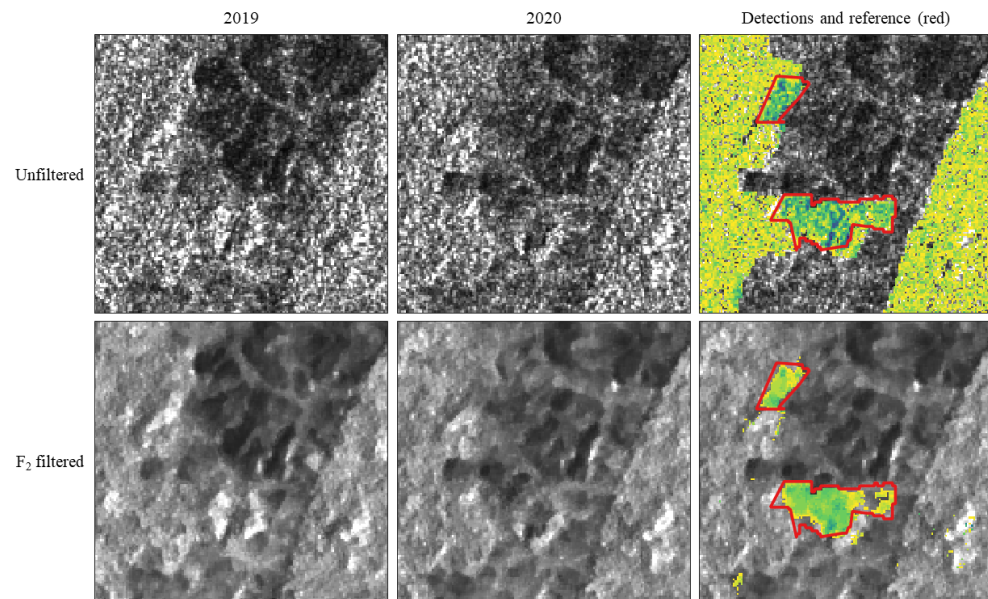
Figure 4. Detail raw and filtered Sentinel-1 images over a 4×4 km^2 area of the Pará site. Notice how speckle filtering reduces the probability of having false deforestation warnings without significantly removing accurate detections.

2.4.1. Time Series Method

The time-series approach used in this paper is analogous to the Adaptive Linear Thresholding (ALT) method introduced in [20], whose central premise is that generally, deforestation will cause a brief but intense decay of the C-band SAR backscattering signal. The method performs pixel-wise dynamic thresholding of the input time series. Firstly, all the available data is divided into a 'learning collection' and a 'detection collection'. Next, the median value of the radar backscattering intensity is computed upon the 'learning collection' for each location. Then, the most recent images, grouped on the 'detection collection', are thresholded against this median value, decreased by a given amount. This given amount, called the 'threshold level', varies as a function of the distance to the nearest past-deforestation, going from -2 dB for the areas closer to past-deforestation, to -3.97 dB, for areas which are more than 5 km apart from previous deforestation.

The thresholding operation will create binary images out of the detection collection, which will be equal to 1 in the corresponding pixel value lower than the threshold level or 0 if it is more significant. When added, these binary images will form a raster image, called a 'detection raster'. This raster will have several attributes, such as the number of detections (i.e., the number of pixels under the threshold), the date of the image that provoked the first detection, and the minimum intensity value below the threshold recorded on the detection collection. Finally, the warning raster is vectorized to create deforestation alert polygons suitable to be sent to enforcement teams in the field. A near real-time deforestation detection system based on this methodology has been made operational by the INPE, under the name DETER-R. A complete description of the system methods and results can be found in [49].

2.4.2. U-Net with Early Fusion

The U-Net architecture employed in this work was adapted from [50]. It follows an encoder–decoder approach, as shown in Figure 5. The encoder comprises a series of convolutions, followed by the rectified linear unit (ReLU) as the activation function and max-pooling operation for down-sampling. The decoder consists of a succession of bilinear up-sampling operations, followed by convolution blocks to map the feature representation back into the spatial resolution of input data. The skip connections bring to the decoder features of corresponding encoder layers. It aims to recover the fine spatial details lost

during the encoder down-sampling steps. Finally, the decoder outputs a tensor containing the posterior class probabilities for each pixel location.
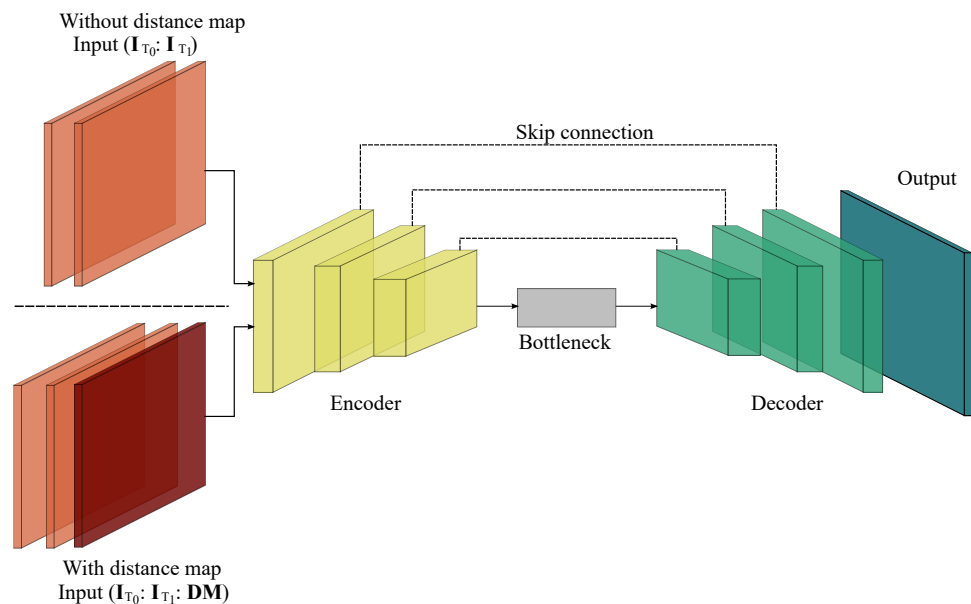

Figure 5. U-Net architecture with convolutional Encoder and Decoder stages. When the distance map is not included, the input is the concatenation of the images $\mathbf{I}_{T_0}$ and $\mathbf{I}_{T_1}$. When the distance map is included, the input is the concatenation of the images $\mathbf{I}_{T_0}$, $\mathbf{I}_{T_1}$ and the distance map (DM).

We adopted the "early fusion" strategy to detect deforestation, which refers to how the input data is combined before classification. Essentially, the input images acquired at dates T_0 and T_1 are stacked along their spectral dimension, resulting in a tensor $\mathbf{I} \in \mathbb{R}^{H \times W \times C}$, where H and W refers to the spatial dimensions and C to the number bands of the images. Moreover, each polarization band (VV and VH) was normalized to zero mean and unit variance before applying the U-Net method. The distance map, if used, is combined with the input data by concatenating it to the tensor defined by the stacked image pair.

2.5. Experimental Setup

The experimental analysis reported in the next section compares the Deep Learning approach, represented by the U-Net configured in the early-fusion scheme, and the time series approach proposed in [20]. For both pixel labeling approaches, we tested six input configurations: the raw input data (R), the spatially filtered data (F_1), the full spatially and temporally filtered data (F_2), the stabilized data (S), the stabilized and spatially filtered (SF_1), and the stabilized and fully spatially and temporally filtered (SF_2). For the time series method, we considered a two-year learning collection. The detection collection was formed with all the available images between $Ref.T_0$ (July 2019) and $Ref.T_1$ (July 2020).

As for the U-Net architecture, we divided the two datasets into tiles: 60 tiles of 961×932 pixels for Pará and 30 tiles comprising 1046×1154 pixels for Mato Grosso. For both datasets, we split the tiles 60%, 20%, and 20% for training, validation, and testing, respectively. The network was trained on image patches of 128×128 pixels cropped from the input image, with a stride equal to 32 pixels and an overlap of 70%. We carried the inference tile-wise. Table 4 shows details of the network architecture implemented for our experiments.

Table 4. U-Net Architecture. Symbols: C (Convolution), MP (Max-pooling), US (Bilinear Up-sampling). The parametrization is (Kernel Height × Kernel Height, Number of filters).

Encoder	Bottleneck	Decoder	Output
MP(C(3 × 3, 32))	2× C(3 × 3, 128)	US(C(3 × 3, 128))	Softmax(C(1 × 1,
MP(C(3 × 3, 64))		US(C(3 × 3, 64))	# Classes))
MP(C(3 × 3, 128))		US(C(3 × 3, 32))	

We followed a cross-validation strategy for the training process, so we randomly split both datasets into 6-folds. In this procedure, we ensured that all tiles were part of the test set only once. Then, the final prediction was a mosaic of the test tiles, which composed the whole image. In addition, we follow this parameter setup: batch size equal to 32, Adam optimizer with learning rate equal to 1×10^{-3}, and β equal to 0.9, and, to avoid over-fitting, an early stopping strategy was employed with a patient equal to 10.

Considering that the dataset is highly unbalanced, we set the weighted cross entropy as a loss function with a vector of weights equals to $[0.1, 0.9]$ for class no-deforestation and deforestation, respectively. Following the PRODES methodology, the class past-deforestation was not considered during training, validation, and testing. To ensure that all the patches contained samples from both classes, we took for training only patches having at least 2% of pixels of deforestation . In addition, a data augmentation procedure for training and validation was applied; these operations included rotation (90°) and flipping (horizontal, vertical) transformations.

Following the PRODES methodology, we ignored pixels within a two-pixel wide buffer at the inner and outer edges of all polygons identified as deforestation in the reference data. These pixels were ignored for training, validation, and testing. Consequently, we set the weight of these pixels to zero in the FCN loss function. In addition, we ignored deforestation polygons smaller than 156 pixels (6.25 ha) for accuracy measurement.

3. Results and Discussion

In this section, we report and analyze the results obtained for the two study sites applying the time series method and the U-Net architecture (described in Section 2). The results are summarized in terms of Mean Average Precision (mAP). In addition, we illustrate the deforested probability maps produced in each experiment.

3.1. Results of Experiments on the Pará Dataset

Figure 6 shows the Precision vs. Recall curves obtained in the experiments on the time series method. The dotted curve represents the results obtained from raw input data, the poorest performance among all input variants. The colourful unbroken lines depict the results from input data after stabilization and filtering. The curves indicate that the combination of stabilization and complete filtering SF_2 achieved the best result (62.7%), followed by SF_1 with a score of 55.5%. With the application of filters, the results improved about 5% compared to the raw (R) and stabilized (S) data, which presented the poorest mAP scores, 47.7% and 51.4%, respectively. Therefore, the stabilization and filtering procedures brought a significant performance gain for the time series method.
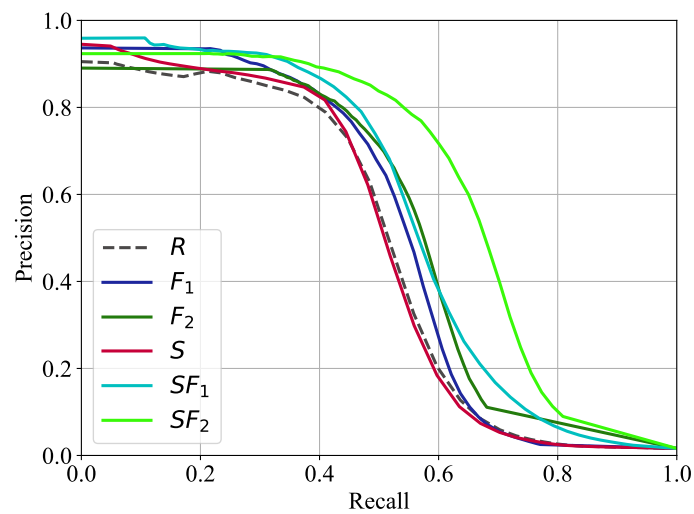
Figure 6. Precision vs. Recall curves for time series method in the Pará site.

Figure 7 presents the Precision vs. Recall curves generated by the U-Net without using the distance maps to the nearest prior deforestation. The mAP values increased significantly for all experiments compared to the time series method. However, contrary to the results recorded for the time series, the best U-Net results were achieved using the stabilized (S) and raw (R) data with 76.3% and 76.1%, respectively. Thus, instead of improving, both forms of filtering detracted from U-Net performance. One possible explanation is that the filtering eliminated useful information for U-Net to differentiate between forested and deforested areas. The stabilization operation, on the contrary, was beneficial. It is worth remembering that the stabilization process aims to eliminate the noise resulting from variations in the canopy moisture. This operation requires accessing a sequence of past images of the same region. In our experiments, the U-Net had no access to this temporal data. Therefore, it could hardly infer such information from its input.
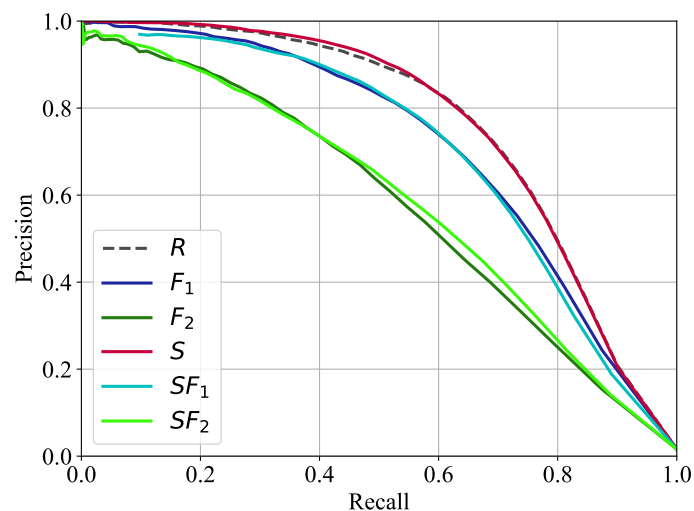

Figure 7. Precision vs. Recall curves for the U-Net architecture in the Pará site.

Next, Figure 8 draws Precision vs. Recall curves when we added the distance map to the closest past-deforestation as an extra input feature. Comparing these curves with the ones of Figure 7, one concludes that the inclusion of the distance map consistently improved the U-Net mAP values between 2.7% and 7.6%, depending on the input data. These results support the hypothesis that deforestation becomes more likely the closer one gets to already deforested areas.
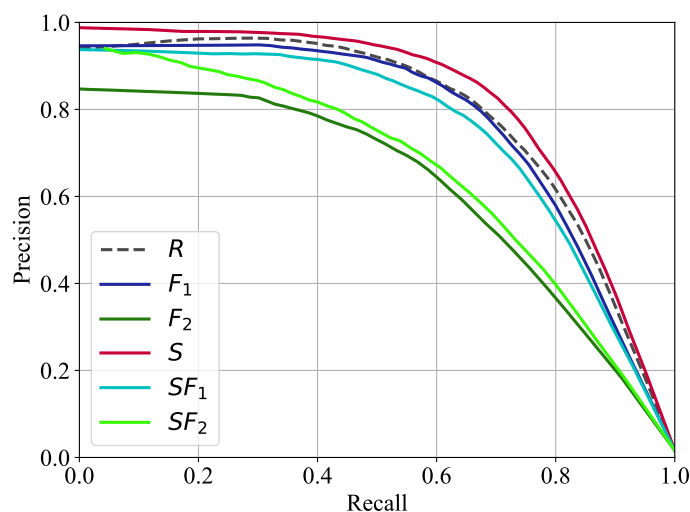
Figure 8. Precision vs. Recall curves for the U-Net architecture with the distance map in the Pará site.

Table 5 summarizes the mAP scores obtained for all experiments on the site located in the Pará state. Values in bold correspond to the best-recorded mAP of each pixel labeling strategy. The superiority of the approach based on the U-Net over the method proposed in [20] becomes evident. Likewise, the table shows that adding the distance map has consistently improved the mAP values.

Table 5. Mean Average Precision (mAP) scores obtained from the evaluated methods in the Pará site.

Image Pair	Time Series	U-Net	U-Net & Distance Map
R	47.7	76.1	78.8
F_1	51.4	71.3	78.9
F_2	53.0	58.0	62.1
S	48.2	**76.3**	**81.8**
SF_1	55.5	70.4	74.8
SF_2	**62.7**	60.0	66.0

Finally, Figure 9 illustrates the probability maps in a snip of the Pará site. This region starts at the point (x_0: 4400, x_1: 2300) and has an extension of 8.4 km^2. In these maps, red and blue represent the highest and the lowest deforestation probability, respectively. Black denotes past-deforested regions, excluded from training and evaluation. Each column exhibits the output from the time series method, U-Net, and U-Net with the distance map to the nearest past-deforestation. Each row refers to the six data variants (R, F_1, F_2, S, SF_1, SF_2). The first image on the top is the ground-truth provided by PRODES with the true labels (Green, deforestation; Red, past-deforestation; Blue, no deforestation). According to this figure, the best results delivered by the time-series method (column on the left) were obtained with the SF_2 treatment (Figure 9p). In this case, the deforested regions were well-defined compared to the other maps, even though a kind of salt-and-pepper noise is observable in the resulting probability map. On the other hand, the probability maps generated from R and S (Figure 9a,j) data contain a lot of wrongly assigned high deforestation probabilities, which were partially eliminated by the filters. The U-Net architecture (middle columns) delivered a much better output than the time-series method, specially for S and R input data variants (Figure 9b,k). In all cases, the salt-and-pepper noise decreased substantially, and higher probability values were produced, denoting more assignment confidence. The distance to the nearest past-deforestation map (right column) improved the results in all scenarios; the deforested polygons had sharper contours, comparatively less intermediate probability values, and, consequently, more confident outcomes.
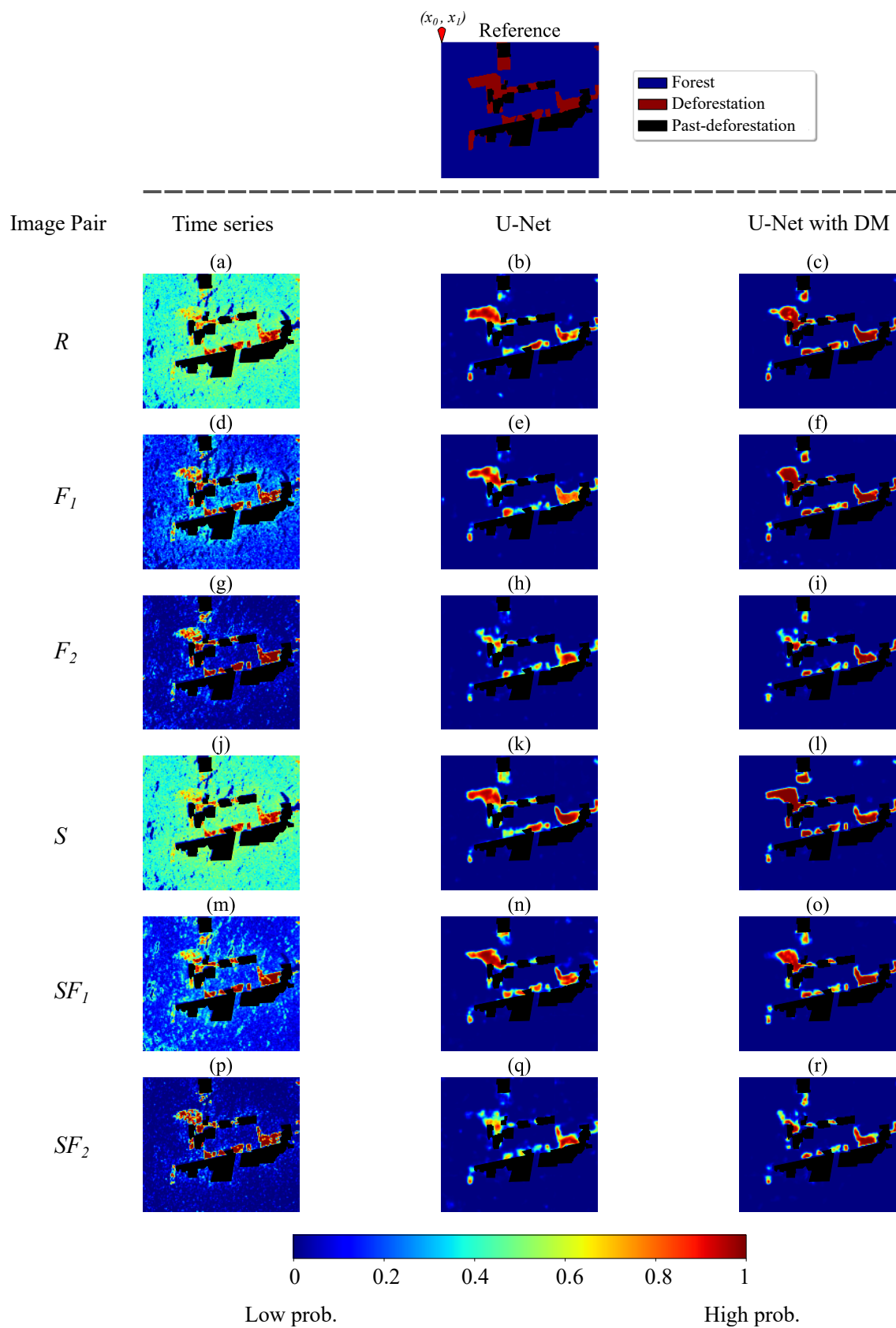
Figure 9. Snip of deforestation probability maps in the Pará site (starting at the point (x_0: 4400, x_1: 2300) and with an extension of 8.4 km^2). Each line represents the raw and the five pre-processing techniques applied to the image pair. The methods evaluated are listed in each column. Blue and red pixels symbolize the lowest and the highest probability of the deforestation class, respectively, and black regions represent past-deforestation.

3.2. Results of Experiments on the Mato Grosso Dataset

Figure 10 presents the Precision vs. Recall curves drawn from the results produced by the time series method. The best results were obtained from filtered input data in both variants (F_2 and F_1), with values around 50.6%. Notice that the performance was inferior to what was recorded in the experiments on the Pará dataset. The reason may be that the Mato Grosso dataset is comparatively more unbalanced, making training more challenging.

It is worth mentioning that the Mato Grosso site lies in the transition of the Amazonia dense forests biome and the Cerrado savannas. Global warming and regional deforestation has provoked a degradation of the forests in this transitional zone (ecotone) [51]. This degradation induces a heavy seasonal component on the forest phenology that will provoke errors in the time-series deforestation detection ATL method, which expects a nearly-constant backscattering signal over dense forests. This degradation will also misguide the harmonic stabilization, as it is designed to control near-sinusoidal seasonality, such as the one provoked by precipitation variation. Seasonality of degraded forests or savannas are modeled using more complex models, as mentioned in [52], such as dual logistic curves [53].
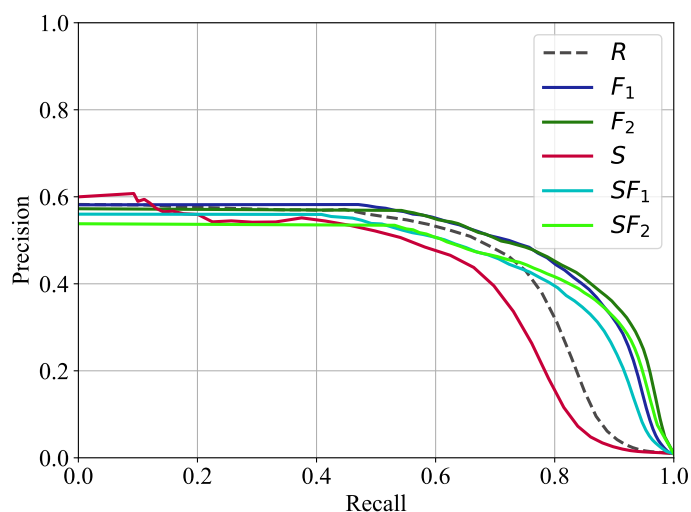

Figure 10. Precision vs. Recall curves for time series method in the Mato Grosso site.

Figure 11 shows the Precision vs. Recall curves obtained by the U-Net, without considering the distance map. The best results correspond to the stabilized data (S), raw (R) and (F_2), in all these cases, values around 57%. Like in the experiments on the Pará site, the U-Net learned a model capable of renouncing data preprocessing with no significant accuracy loss. Besides this, although less markedly than for the Pará site, U-Net performed better than the time series method for all input variants and also for the Mato Grosso site.

Figure 12 shows the U-Net results generated after including the distance map. Similar to the experiment on the Pará site with the same input, the Precision vs. Recall curves reveal that the distance map brought mAP improvements around 3% to 4% in all these cases.
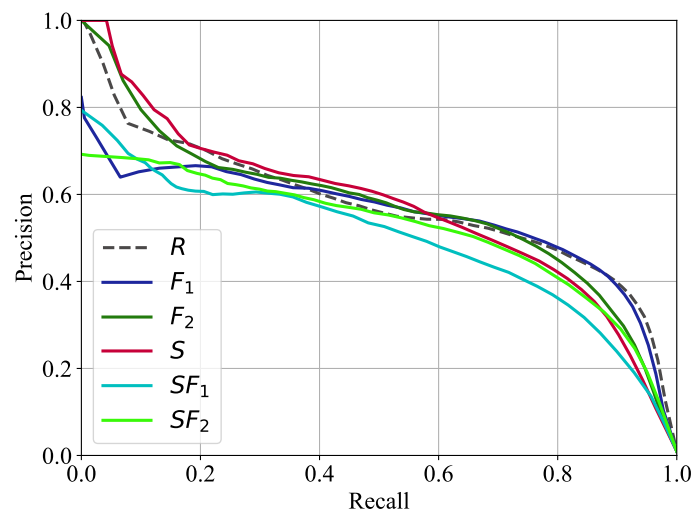
Figure 11. Precision vs. Recall curves for the U-Net architecture in the Mato Grosso site.
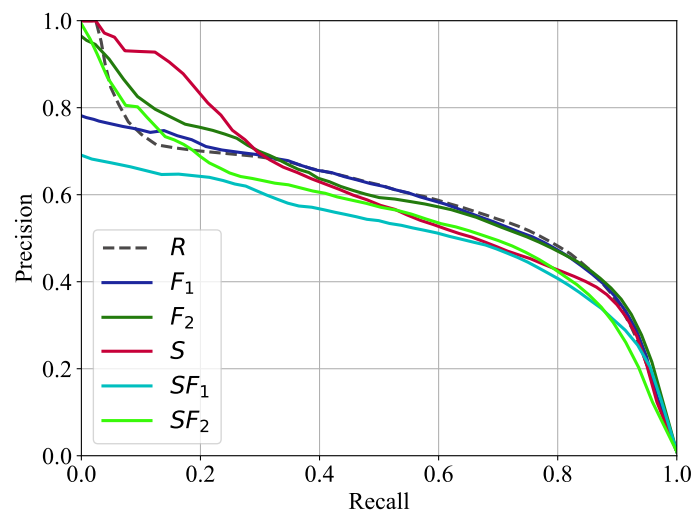

Figure 12. Precision vs. Recall curves for the U-Net architecture with the distance map in the Mato Grosso site.

Table 6 summarizes the mAP scores obtained in all experiments carried out on Mato Grosso dataset.

Table 6. Mean Average Precision (mAP) scores obtained from the evaluated methods in the Mato Grosso site.

Image Pair	Time Series	U-Net	U-Net & Distance Map
R	45.5	57.4	59.2
F_1	50.4	55.2	58.3
F_2	**50.6**	57.2	60.1
S	41.3	**57.7**	**60.1**
SF_1	46.7	49.4	51.2
SF_2	47.0	52.0	55.5

Figure 13 presents the probability maps in a snip of the Mato Grosso site. This region starts at the point (x_0: 3000, x_1: 500) and has an extension of 30 km^2. As in Figure 9, columns refer to pixel labeling methods, specifically, the time series, the U-Net, and the U-Net with the distance map of past-deforestation. Each row corresponds to an input data variant (R, F_1, F_2, S, SF_1, SF_2). Notice that the time series method (left column) assigned a high

probability to a large portion of pixels belonging to the no-deforestation class. The U-Net (middle column) produced the best probability maps when working on *R* and *F*2 and *S* (Figure 13b,h,k) the input data variants. Although a high probability has been assigned to most deforested regions, some were still nearly barely recognized. Furthermore, the inclusion of the distance map improved all results (right column) by assigning higher probabilities to deforestation spots. These results confirm the conclusion drawn from the experiments on the Pará site that the distance map helps improve deforestation detection accuracy.
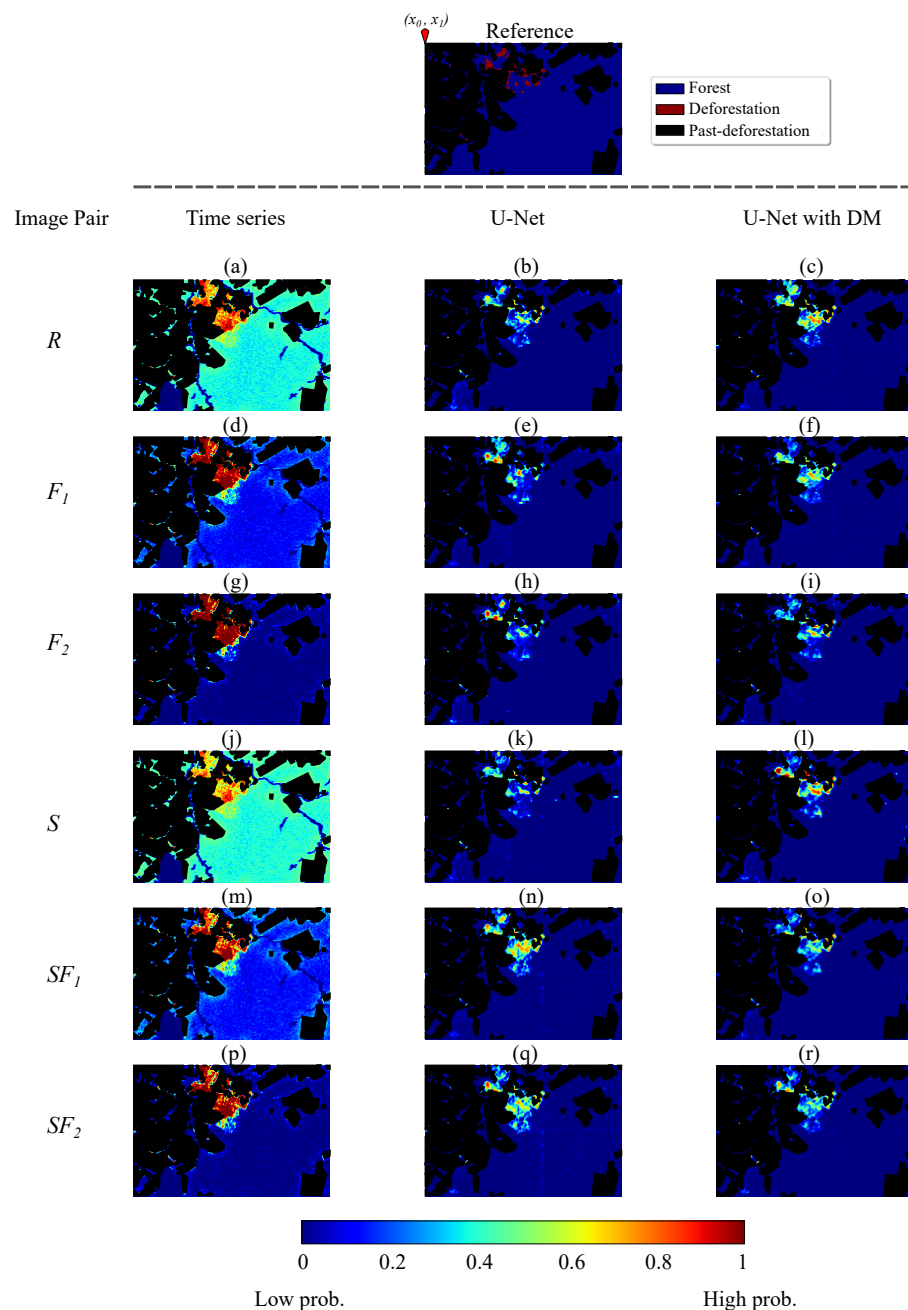

Figure 13. Snip of deforestation probability maps in the Mato Grosso site. Starting at the point (x_0: 3000, x_1: 500) and with an extension of 30 km^2. Each line represents the raw and the five pre-processing techniques applied to the image pair. The methods evaluated are listed in each column. Blue and red pixels symbolize the lowest and the highest probability of the deforestation class, respectively, and black regions represent past-deforestation.

4. Conclusions

This paper reported the results of a study that evaluated the benefits of pre-processing techniques for detecting deforestation from a pair of bi-temporal SAR images employing a fully convolutional network. As pre-processing techniques, we tested a stabilization operation aiming to suppress the effect of seasonal variation in trees' canopy moisture from the compared SAR images. We also applied a combination of a temporal and a spatial filter to the SAR images, aiming to reduce the speckle noise. A U-Net in the early-fusion configuration was used for the pixel-wise classification. As a baseline, we adopted a recent non-deep learning approach that exploits information contained in a sequence of co-registered multitemporal SAR images. Driven by the empirical observation that points closer to previously deforested areas are more prone to deforestation in the near future, the work also proposed and evaluated the benefits of adding to the U-Net input the information regarding the distance of each pixel to its nearest deforested site.

The U-Net outperformed the time-series method in all experiments, with gains above 10%. Furthermore, the results confirmed that speckle filtering is almost mandatory for the time-series approach. However, the U-Net managed to handle the speckle noise and possibly even take advantage of information that said filtering approaches might suppress. As for the pre-processing techniques, the stabilization procedure helped improve the U-Net accuracy. This can be explained by the fact that the stabilization operation uses the information contained in a multitemporal series of co-registered images. Thus, stabilization brings additional information to the network, which is most likely not present in the pair of images applied to the U-Net input. Unlike stabilization, filtering operations brought no accuracy gain and, in many cases, it was even deleterious.

The main challenge for the U-Net was the high data imbalance characteristic of deforestation detection applications. Indeed, the percentage of class deforestation ranged in our datasets between 1% and 0.6%. Despite using a weighted loss, we did not manage to mitigate the problem entirely. Indeed, U-Net performed worse in experiments on the most unbalanced dataset. However, it was consistently superior to the time series approach, even in this case.

This work also proposed providing the network with information regarding the distance of each pixel to its nearest prior deforested site, besides the pair of temporal SAR images. Such additional information consistently improved the U-Net mean Average Precision by 4%.

The experiments revealed that the stabilization process was able to bring significant gains in one of the sites that made up our dataset. Stabilization seeks to capture seasonal variations in tree canopy moisture. Such observation suggests using recurrent networks as an alternative to the stabilization method tested in this study. Finally, it is worth mentioning that the choice of U-Net was mainly due to its wide use in semantic segmentation tasks. Better results are potentially achievable with more elaborate, fully convolutional network architectures. Such questions can be the subject of future works.

Author Contributions: Conceptualization, methodology, M.O.A., J.D.P., R.Q.F. and C.A.D.A.; experiments, writing, and original draft preparation, M.O.A. and J.D.P.; overall study design, co-supervision, writing, review and editing, R.Q.F. and C.A.D.A.; writing—original draft preparation, M.O.A. and J.D.P.; writing—review and editing, R.Q.F. and C.A.D.A.; supervision, R.Q.F. and C.A.D.A. All authors have read and agreed to the published version of the manuscript.

Data Availability Statement: The reference used in this work was downloaded from the databse of the Program for Deforestation Monitoring in the Brazilian Legal Amazon (PRODES) at http://terrabrasilis.dpi.inpe.br/ (accessed on 20 May 2022).

Conflicts of Interest: The authors declare no conflict of interest.

References

1. Nobre, C.A.; Sampaio, G.; Borma, L.S.; Castilla-Rubio, J.C.; Silva, J.S.; Cardoso, M. Land-use and climate change risks in the Amazon and the need of a novel sustainable development paradigm. *Proc. Natl. Acad. Sci. USA* **2016**, *113*, 10759–10768. [CrossRef] [PubMed]
2. Morris, R.J. Anthropogenic impacts on tropical forest biodiversity: A network structure and ecosystem functioning perspective. *Philos. Trans. R. Soc. B Biol. Sci.* **2010**, *365*, 3709–3718. [CrossRef]
3. Almeida, C.A.D.; Coutinho, A.C.; Esquerdo, J.C.D.M.; Adami, M.; Venturieri, A.; Diniz, C.G.; Dessay, N.; Durieux, L.; Gomes, A.R. High spatial resolution land use and land cover mapping of the Brazilian Legal Amazon in 2008 using Landsat-5/TM and MODIS data. *Acta Amaz.* **2016**, *46*, 291–302. [CrossRef]
4. Gomes, V.H.; Vieira, I.C.; Salomão, R.P.; ter Steege, H. Amazonian tree species threatened by deforestation and climate change. *Nat. Clim. Chang.* **2019**, *9*, 547–553. [CrossRef]
5. Pereira, E.J.d.A.L.; de Santana Ribeiro, L.C.; da Silva Freitas, L.F.; de Barros Pereira, H.B. Brazilian policy and agribusiness damage the Amazon rainforest. *Land Use Policy* **2020**, *92*, 104491. [CrossRef]
6. Sano, E.E.; Rizzoli, P.; Koyama, C.N.; Watanabe, M.; Adami, M.; Shimabukuro, Y.E.; Bayma, G.; Freitas, D.M. Comparative analysis of the global forest/non-forest maps derived from SAR and optical sensors. Case studies from Brazilian Amazon and Cerrado biomes. *Remote Sens.* **2021**, *13*, 367. [CrossRef]
7. Xu, X.; Zhang, X.; Riley, W.J.; Xue, Y.; Nobre, C.A.; Lovejoy, T.E.; Jia, G. Deforestation triggering irreversible transition in Amazon hydrological cycle. *Environ. Res. Lett.* **2022**, *17*, 034037. [CrossRef]
8. Tarazona, Y.; Zabala, A.; Pons, X.; Broquetas, A.; Nowosad, J.; Zurqani, H.A. Fusing Landsat and SAR Data for Mapping Tropical Deforestation through Machine Learning Classification and the PVts-β Non-Seasonal Detection Approach. *Can. J. Remote Sens.* **2021**, *47*, 677–696. [CrossRef]
9. Watanabe, M.; Koyama, C.N.; Hayashi, M.; Nagatani, I.; Shimada, M. Early-stage deforestation detection in the tropics with L-band SAR. *IEEE J. Sel. Top. Appl. Earth Obs. Remote Sens.* **2018**, *11*, 2127–2133. [CrossRef]
10. Hansen, M.C.; Krylov, A.; Tyukavina, A.; Potapov, P.V.; Turubanova, S.; Zutta, B.; Ifo, S.; Margono, B.; Stolle, F.; Moore, R. Humid tropical forest disturbance alerts using Landsat data. *Environ. Res. Lett.* **2016**, *11*, 034008. Available online: http://www.glad.umd.edu/ (accessed on 10 May 2022). [CrossRef]
11. Diniz, C.G.; Souza, A.A.D.A.; Santos, D.C.; Dias, M.C.; Luz, N.C.D.; Moraes, D.R.V.D.; Maia, J.S.A.; Gomes, A.R.; Narvaes, I.D.S.; Valeriano, D.M.; et al. DETER-B: The New Amazon Near Real-Time Deforestation Detection System. *IEEE J. Sel. Top. Appl. Earth Obs. Remote Sens.* **2015**, *8*, 3619–3628. [CrossRef]
12. Danklmayer, A.; Doring, B.J.; Schwerdt, M.; Chandra, M. Assessment of atmospheric propagation effects in SAR images. *IEEE Trans. Geosci. Remote Sens.* **2009**, *47*, 3507–3518. [CrossRef]
13. Soares-Filho, B.; Moutinho, P.; Nepstad, D.; Anderson, A.; Rodrigues, H.; Garcia, R.; Dietzsch, L.; Merry, F.; Bowman, M.; Hissa, L.; et al. Role of Brazilian Amazon protected areas in climate change mitigation. *Proc. Natl. Acad. Sci. USA* **2010**, *107*, 10821–10826. [CrossRef]
14. Assunção, J.; Gandour, C.; Rocha, R. DETERring deforestation in the Brazilian Amazon: Environmental monitoring and law enforcement. *Clim. Policy Initiat.* **2013**, *1*, 36.
15. Nepstad, D.; McGrath, D.; Stickler, C.; Alencar, A.; Azevedo, A.; Swette, B.; Bezerra, T.; DiGiano, M.; Shimada, J.; da Motta, R.S.; et al. Slowing Amazon deforestation through public policy and interventions in beef and soy supply chains. *Science* **2014**, *344*, 1118–1123. [CrossRef]
16. Park, N.W.; Chi, K.H. Integration of multitemporal/polarization C-band SAR data sets for land-cover classification. *Int. J. Remote Sens.* **2008**, *29*, 4667–4688. [CrossRef]
17. Trisasongko, B.H. The use of polarimetric SAR data for forest disturbance monitoring. *Sens. Imaging Int. J.* **2010**, *11*, 1–13. [CrossRef]
18. Jia, M.; Wang, L. Novel class-relativity non-local means with principal component analysis for multitemporal SAR image change detection. *Int. J. Remote Sens.* **2018**, *39*, 1068–1091. [CrossRef]
19. Hethcoat, M.G.; Carreiras, J.M.; Edwards, D.P.; Bryant, R.G.; Quegan, S. Detecting tropical selective logging with C-band SAR data may require a time series approach. *Remote Sens. Environ.* **2021**, *259*, 112411. [CrossRef]
20. Doblas, J.; Shimabukuro, Y.; Sant'Anna, S.; Carneiro, A.; Aragão, L.; Almeida, C. Optimizing near real-time detection of deforestation on tropical rainforests using sentinel-1 data. *Remote Sens.* **2020**, *12*, 3922. [CrossRef]
21. Hoekman, D.; Kooij, B.; Quiñones, M.; Vellekoop, S.; Carolita, I.; Budhiman, S.; Arief, R.; Roswintiarti, O. Wide-area near-real-time monitoring of tropical forest degradation and deforestation using Sentinel-1. *Remote Sens.* **2020**, *12*, 3263. [CrossRef]
22. Mermoz, S.; Bouvet, A.; Koleck, T.; Ballère, M.; Le Toan, T. Continuous Detection of Forest Loss in Vietnam, Laos, and Cambodia Using Sentinel-1 Data. *Remote Sens.* **2021**, *13*, 4877. [CrossRef]
23. Nicolau, A.P.; Flores-Anderson, A.; Griffin, R.; Herndon, K.; Meyer, F.J. Assessing SAR C-band data to effectively distinguish modified land uses in a heavily disturbed Amazon forest. *Int. J. Appl. Earth Obs. Geoinf.* **2021**, *94*, 102214. [CrossRef]
24. Hethcoat, M.G.; Carreiras, J.M.; Edwards, D.P.; Bryant, R.G.; Quegan, S. Detecting tropical selective logging with SAR data requires a time series approach. *bioRxiv* **2020**. [CrossRef]
25. Diniz, J.M.F.D.S.; Gama, F.F.; Adami, M. Evaluation of polarimetry and interferometry of Sentinel-1A SAR data for land use and land cover of the Brazilian Amazon region. *Geocarto Int.* **2020**, *37*, 1482–1500. [CrossRef]

26. Hansen, J.N.; Mitchard, E.T.; King, S. Assessing forest/non-forest separability using Sentinel-1 C-Band synthetic aperture radar. *Remote Sens.* **2020**, *12*, 1899. [CrossRef]
27. Lu, D.; Mausel, P.; Brondízio, E.; Moran, E. Change detection techniques. *Int. J. Remote Sens.* **2004**, *25*, 2365–2401. [CrossRef]
28. Parrilli, S.; Poderico, M.; Angelino, C.V.; Verdoliva, L. A nonlocal SAR image denoising algorithm based on LLMMSE wavelet shrinkage. *IEEE Trans. Geosci. Remote Sens.* **2011**, *50*, 606–616. [CrossRef]
29. Assis, F.; Fernando, L.; Ferreira, K.R.; Vinhas, L.; Maurano, L.; Almeida, C.; Carvalho, A.; Rodrigues, J.; Maciel, A.; Camargo, C. A Tutorial on Speckle Reduction in Synthetic Aperture Radar Images. *ISPRS Int. J. Geo-Inf.* **2013**, *1*, 6–35.
30. Cozzolino, D.; Parrilli, S.; Scarpa, G.; Poggi, G.; Verdoliva, L. Fast adaptive nonlocal SAR despeckling. *IEEE Geosci. Remote Sens. Lett.* **2013**, *11*, 524–528. [CrossRef]
31. Penna, P.A.; Mascarenhas, N.D. SAR speckle nonlocal filtering with statistical modeling of HAAR wavelet coefficients and stochastic distances. *IEEE Trans. Geosci. Remote Sens.* **2019**, *57*, 7194–7208. [CrossRef]
32. Ma, L.; Liu, Y.; Zhang, X.; Ye, Y.; Yin, G.; Johnson, B.A. Deep learning in remote sensing applications: A meta-analysis and review. *ISPRS J. Photogramm. Remote Sens.* **2019**, *152*, 166–177. [CrossRef]
33. Yuan, Q.; Shen, H.; Li, T.; Li, Z.; Li, S.; Jiang, Y.; Xu, H.; Tan, W.; Yang, Q.; Wang, J.; et al. Deep learning in environmental remote sensing: Achievements and challenges. *Remote Sens. Environ.* **2020**, *241*, 111716. [CrossRef]
34. Vali, A.; Comai, S.; Matteucci, M. Deep learning for land use and land cover classification based on hyperspectral and multispectral earth observation data: A review. *Remote Sens.* **2020**, *12*, 2495. [CrossRef]
35. Srivastava, V.; Biswas, B. CNN-based salient features in HSI image semantic target prediction. *Connect. Sci.* **2020**, *32*, 113–131. [CrossRef]
36. Adarme, M.O.; Feitosa, R.Q.; Happ, P.N.; De Almeida, C.A.; Gomes, A.R. Evaluation of deep learning techniques for deforestation detection in the Brazilian Amazon and cerrado biomes from remote sensing imagery. *Remote Sens.* **2020**, *12*, 910. [CrossRef]
37. De Bem, P.P.; de Carvalho Junior, O.A.; Guimarães, R.F.; Gomes, R.A.T. Change detection of deforestation in the Brazilian Amazon using landsat data and convolutional neural networks. *Remote Sens.* **2020**, *12*, 901. [CrossRef]
38. Adarme, M.O.; Costa, G.; Feitosa, R. Multi-Attention Ghostnet for Deforestation Detection in the Amazon Rainforest. *ISPRS Ann. Photogramm. Remote Sens. Spat. Inf. Sci.* **2022**, *3*, 657–664. [CrossRef]
39. Silva, C.A.; Guerrisi, G.; Del Frate, F.; Sano, E.E. Near-real time deforestation detection in the Brazilian Amazon with Sentinel-1 and neural networks. *Eur. J. Remote Sens.* **2022**, *55*, 129–149. [CrossRef]
40. Kuck, T.N.; Silva Filho, P.F.F.; Sano, E.E.; Bispo, P.D.C.; Shiguemori, E.H.; Dalagnol, R. Change Detection of Selective Logging in the Brazilian Amazon Using X-Band SAR Data and Pre-Trained Convolutional Neural Networks. *Remote Sens.* **2021**, *13*, 4944. [CrossRef]
41. Wahab, M.A.A.; Surin, E.S.M.; Nayan, N.M. An Approach to Mapping Deforestation in Permanent Forest Reserve Using the Convolutional Neural Network and Sentinel-1 Synthetic Aperture Radar. In Proceedings of the 2021 Fifth International Conference on Information Retrieval and Knowledge Management (CAMP), Kuala Lumpur, Malaysia, 15–16 June 2021; pp. 59–64.
42. Assis, F.; Fernando, L.; Ferreira, K.R.; Vinhas, L.; Maurano, L.; Almeida, C.; Carvalho, A.; Rodrigues, J.; Maciel, A.; Camargo, C. TerraBrasilis: A Spatial Data Analytics Infrastructure for Large-Scale Thematic Mapping. *ISPRS Int. J. Geo-Inf.* **2019**, *8*, 513. [CrossRef]
43. Gorelick, N.; Hancher, M.; Dixon, M.; Ilyushchenko, S.; Thau, D.; Moore, R. Google Earth Engine: Planetary-scale geospatial analysis for everyone. *Remote Sens. Environ.* **2017**, *202*, 18–27. [CrossRef]
44. National Institute for Space Research. General Coordination of Earth Observation. Monitoring Program for the Amazon and Other Biomes. Deforestation-Legal Amazon. Available online: http://terrabrasilis.dpi.inpe.br (accessed on 20 May 2022).
45. Reiche, J.; Verhoeven, R.; Verbesselt, J.; Hamunyela, E.; Wielaard, N.; Herold, M. Characterizing tropical forest cover loss using dense Sentinel-1 data and active fire alerts. *Remote Sens.* **2018**, *10*, 777. [CrossRef]
46. Quegan, S.; Yu, J.J. Filtering of multichannel SAR images. *IEEE Trans. Geosci. Remote Sens.* **2001**, *39*, 2373–2379. [CrossRef]
47. Lee, J.S. Refined filtering of image noise using local statistics. *Comput. Graph. Image Process.* **1981**, *15*, 380–389. [CrossRef]
48. Lee, J.S. Speckle analysis and smoothing of synthetic aperture radar images. *Comput. Graph. Image Process.* **1981**, *17*, 24–32. [CrossRef]
49. Doblas, J.; Lima, L.; Mermoz, S.; Bouvet, A.; Reiche, J.; Watanabe, M.; Sant'Anna, S.; Shimabukuro, Y. Inter-comparison of optical and SAR-based forest disturbance warning systems in the Amazon shows the potential of combined SAR-optical monitoring. *Int. J. Remote Sens.* 2022, *submitted*.
50. Ronneberger, O.; Fischer, P.; Brox, T. U-net: Convolutional networks for biomedical image segmentation. In Proceedings of the International Conference on Medical Image Computing and Computer-Assisted Intervention, Munich, Germany, 5–9 October 2015; pp. 234–241.
51. Coe, M.T.; Marthews, T.R.; Costa, M.H.; Galbraith, D.R.; Greenglass, N.L.; Imbuzeiro, H.M.; Levine, N.M.; Malhi, Y.; Moorcroft, P.R.; Muza, M.N.; et al. Deforestation and climate feedbacks threaten the ecological integrity of south-southeastern Amazonia. *Philos. Trans. R. Soc. B Biol. Sci.* **2013**, *368*, 20120155. [CrossRef]
52. Zhou, J.; Jia, L.; Menenti, M.; Gorte, B. On the performance of remote sensing time series reconstruction methods–A spatial comparison. *Remote Sens. Environ.* **2016**, *187*, 367–384. [CrossRef]
53. Li, X.; Zhou, Y.; Meng, L.; Asrar, G.R.; Lu, C.; Wu, Q. A dataset of 30 m annual vegetation phenology indicators (1985–2015) in urban areas of the conterminous United States. *Earth Syst. Sci. Data* **2019**, *11*, 881–894. [CrossRef]